

# Automatic Annotation of Planetary Surfaces With Geomorphic Labels

Soumya Ghosh, Tomasz F. Stepinski, and Ricardo Vilalta

**Abstract**—In this paper, we present a methodology for automatic geomorphic mapping of planetary surfaces that incorporates machine-learning techniques. Our application transforms remotely sensed topographic data gathered by orbiting satellites into semantically meaningful maps of landforms; such maps are valuable research tools for planetary science. As topographic data become increasingly available, the ability to derive geomorphic maps efficiently is becoming essential. In our proposed framework, the mapping is achieved by means of scene segmentation followed by supervised classification of segments. The two mapping steps use different sets of features derived from digital elevation models of planetary surfaces; selection of appropriate features is discussed. Using a particular set of terrain attributes relevant to annotating cratered terrain on Mars, we investigate the design choices for both segmentation and classification components. The segmentation assessment includes  $K$ -means-based agglomerative segmentation and watershed-based segmentation. The classification assessment includes three supervised learning algorithms: Naive Bayes, Bagging with decision trees, and support-vector machines (SVMs); segments are classified into the following landforms: crater floors, crater walls (concave and convex), ridges (concave and convex), and intercrater plains. The method is applied to six test sites on Mars. The analysis of the results shows that a combination of  $K$ -means-based agglomerative segmentation and either SVM with a quadratic kernel or Bagging with C4.5 yields best maps. The presented framework can be adopted to generate geomorphic maps of sites on Earth.

**Index Terms**—Classification, digital topography, Mars, object recognition, segmentation.

## I. INTRODUCTION

REMOTE-SENSING instruments onboard spacecraft are providing increasingly large volumes of data on various aspects of Earth as well as surfaces of other planets. This data-rich environment challenges the scientific community to process, analyze, and ultimately turn into knowledge a significant portion of all collected data. In the context of planetary science, most data need to be presented in the context of geomorphic maps [48]—basic staples of any planetary geology

Manuscript received December 16, 2008; revised June 2, 2009. First published September 9, 2009; current version published December 23, 2009. This work was supported by the National Science Foundation under Grants IIS-0431130, IIS-448542, and IIS-0430208 and in part by the National Aeronautics and Space Administration under Grant NNG06GE57G.

S. Ghosh is with the University of Colorado at Boulder, Boulder, CO 80309 USA (e-mail: soumya.ghosh@colorado.edu).

T. F. Stepinski is with the Lunar and Planetary Institute, Houston, TX 77058-1113 USA (e-mail: tom@lpi.usra.edu).

R. Vilalta is with the University of Houston, Houston, TX 77204-3010 USA (e-mail: vilalta@cs.uh.edu).

Color versions of one or more of the figures in this paper are available online at <http://ieeexplore.ieee.org>.

Digital Object Identifier 10.1109/TGRS.2009.2027113

research. A geomorphic map is a categorical (thematic) map of topographical expressions (landforms). Traditionally, such maps are drawn by analysts through visual interpretations of images [42], [48].

In this paper, we present a methodology for automating the process of geomorphic mapping. We are motivated by the slowness and expense of the traditional mapping process. If left to manual mapping, the percentage of planetary surface mapped to the level of detail permitted by an increased resolution of newly arriving data will continue to drop precipitously. Automating the mapping process can prevent this decline. We use topographic data as input for machine mapping, because landforms can be better characterized by topographic features than by image features. Our method relies on segmentation-based classification of a landscape scene into constituent landforms. Such an approach yields results that, in their appearance and content, mimic manually derived maps.

## A. Background

The overwhelming majority of previous work on automatic annotation of remotely sensed data was devoted to classification of multispectral images into different types of land covers. A standard approach to classification of raster data [images or digital elevation models (DEMs)] is to use pixels as objects for classification [22], [23]. However, a pixel is not an ideal surface unit from the point of view of classification. Real-life objects are characterized by a similarity of color and texture rather than a similarity of color alone. This observation led to the technique of segmentation-based classification wherein an image is first subdivided into meaningful objects that are subsequently classified [27], [45]. As a general rule, the segmentation-based approach produces better maps from images than the pixel-based approach [20]. The segmentation-based approach is even more attractive when working with topographic instead of imagery data. Pixels are just too small to constitute reasonable landscape elements; larger patches of surface better reflect local topographic expressions. This is important for supervised classification, where a domain expert must label each unit in a training set. Furthermore, geometric and statistical properties of landscape elements, such as shape, neighborhood properties, and statistics corresponding to terrain attributes calculated over an ensemble of member pixels, provide additional information that can be incorporated into classification.

The topic of automapping landforms from topography has received little attention in the past, but with the introduction of segmentation-based classification methods, there is now a renewed interest in such mapping [13], [15]. However, published

approaches rely on hand-made rules for classification and fail to take advantage of machine-learning techniques.

### B. Related Work

In the past, automapping of planetary surfaces was restricted to identifying particular targets of interest, namely, impact craters [2], [3], [9], [10], [17], [21], [24], [25], [30], [34], [35], [47]. Machine crater identification could be considered an example of machine mapping, albeit a simple one, containing a single landform. In contrast, this paper has been directed toward the automatic generation of geomorphic maps that contain several landforms. Our efforts have concentrated on planet Mars because Mars is the only planet besides Earth for which global topographic data are currently available [38]. In [8] and [39], we explored pixel-based unsupervised learning for mapping landforms. Such an approach required a significant manual postclustering processing phase to interpret the output clusters and produce a map amenable to interpretation by a planetary analyst. The analyst had no control over the classes of landforms expressed in the resulting map, and the interpreted classes lacked customary geomorphic meaning, thus limiting the practical use of the map. This occurs because a reasonable cluster derived under a proximity measure may not constitute a customary landform as perceived by a human analyst. Recognizing that appearance and content of automatically generated maps must mimic manually derived maps; we have started to explore the concatenation of a segmentation-based technique with supervised learning [40], [41] as a framework for geomorphic mapping.

### C. Preface

In this paper, we propose a unifying framework for annotating planetary surfaces with geomorphic labels. This framework is based on segmentation-based supervised learning. We utilize such framework for annotation of a particular surface—a cratered terrain on planet Mars. We assess and discuss the use of two different segmentation algorithms designed to procure small segments required for accurate classification. We also assess three supervised learning algorithms for the purpose of classifying segments into desired landform classes. Landform classification is challenging because different landforms of interest may be characterized by similar local terrain features but have different semantic meanings due to their spatial context. We address this issue by incorporating neighborhood information as segment-based features.

The rest of this paper is organized as follows. Section II describes the input data and feature-selection step. In Section III, we present our approach to scene segmentation; Section IV describes the classification techniques. Experimental results are shown and discussed in Section V, followed by conclusions and future research directions in Section VI.

## II. DATA SET AND PIXEL-BASED FEATURES

Our method is contingent on the availability of topographic data. In the near future, such data will become available for



Fig. 1. Topography of the Tisia test site on Mars.

the Moon and planet Mercury, but presently, Mars is the only planet (other than the Earth) for which global topography is available. Raw data used in this paper were gathered by the Mars Orbiter Laser Altimeter instrument [38] onboard the Mars Global Surveyor spacecraft. The data are organized in the form of a DEM, a raster data set where each pixel is assigned an elevation value. The global Martian DEM has a resolution of 128 pixels per degree ( $\sim 460$  m at the equator).

We demonstrate the performance of our method by generating geomorphic maps for several sites on Mars referred to as Tisia, Al-Qahira, Dawes, Evros, Margaritifer, and Vichada. The Tisia site, centered at  $46.13^\circ$  E,  $11.83^\circ$  S, is our primary study area; it will be used to demonstrate the components of our framework and will serve as the training site. It was chosen as the primary site because it contains all the landforms of interest in a relatively small area. Moreover, the same site was previously studied in [39], [41], and [44], so our present mapping can be directly compared with previous results. The DEM of Tisia site has dimensions of 385 rows and 424 columns and is shown in Fig. 1.

We generate a geomorphic map expressing the following landforms: crater floors, crater walls, ridges, and intercrater plains. Crater walls and ridges are further categorized into convex and concave depending on their curvature. Lower regions of walls and ridges have positive curvature and are termed convex. On the other hand, higher regions of walls and ridges have negative curvature and are termed concave. Overall, we aim at mapping six landform classes: crater floors, convex crater walls, concave crater walls, convex ridges, concave ridges, and intercrater plateau. The choice of these particular landform classes stems from our interest in the automatic characterization of cratered surfaces. Other landforms could be chosen depending on the application of interest.

The DEM carries information about terrain elevation,  $z(x, y)$  at the location  $(x, y)$  of each pixel. However, elevation is not a variable well suited to discriminate between the aforementioned landform classes. Instead, we use the DEM to calculate other terrain attributes.

- 1) *Slope*—Slope  $s(x, y)$  defines the rate of maximum change of  $z$  on the  $3 \times 3$  neighborhood of a pixel. A slope is a useful feature for delineating crater walls and ridges.
- 2) *Curvature*—The tangential curvature [28]  $\kappa(x, y)$  measures the change of the slope angle in the direction of tangent to contour and is calculated analytically from a fourth-order polynomial fitted to a patch of surface composed of a  $3 \times 3$  neighborhood centered on a focus pixel. Curvature is used for distinguishing between convex and concave crater walls and ridges.  $\kappa > 0$  corresponds to convex topography, whereas  $\kappa < 0$  corresponds to concave topography.
- 3) *Flood*—Flood  $f(x, y)$  is a binary variable such that pixels located inside topographic basins have  $f(x, y) = 1$ , and all other pixels have  $f(x, y) = 0$ . The flood variable is particularly useful to distinguish between two flat landforms, intercrater plateaus, and crater floors, because crater floors are usually enclosed basins, and plateaus are not.

A pixel-based feature vector,  $v(x, y) = \{s, \kappa, f\}(x, y)$ , describes the topography of the landscape at the level of an individual pixel. The raster of vectors  $v$  offers a mathematical representation of a site's landscape. Pixel-based feature vectors are used in the segmentation stage of our proposed method.

### III. SEGMENTATION

Segmentation is an intermediate data-preparation stage in our framework. The segmentation procedure subdivides the landscape into mutually exclusive and exhaustive segments containing pixels having approximately uniform feature vectors. These segments constitute topographic objects, which are classified and merged into coherent physical landforms by the supervised learning algorithms applied in the later stages of our framework. Raster segmentation has been the subject of intense study in the domain of image analysis. In the context of image analysis, a variety of techniques have been proposed [1], [4], [11], [14], [29], [37], [46], all of which could, in principle, be extended to landscape segmentation. However, requirements for an effective segmentation for the purpose of classification are different from those encountered in the field of computer vision. In particular, for the purpose of classification, it is desirable to have relatively small approximately equal-sized segments (a requirement at odds with typical problems in image analysis). Having small segments eliminates the danger of a particularly large segment being misclassified, which would avoid producing a grossly incorrect map. Additionally, a misclassification of a small segment carries a small impact in the overall map accuracy. Moreover, having approximately equal-sized segments assures that statistics of terrain attributes are calculated from comparable ensembles of member pixels.

We investigate two different segmentation algorithms. The dividing algorithm splits the landscape on the basis of abrupt discontinuities in pixel-based feature vectors. The agglomerative algorithm initially treats each pixel as an individual segment. These initial segments are combined into larger segments as long as a user-defined criterion for the uniformity of

constituent pixel-based feature vectors holds. Both algorithms use the same pixel-based feature vectors  $v(x, y)$ .

#### A. Watershed-Based Segmentation

Our first approach to segmenting a landscape incorporates the watershed transform [5] applied to a grayscale image that encapsulates gradients of pixel-based feature vectors. This image is calculated using a (computationally simple) homogeneity measure  $H$  [18]. The homogeneity measure  $H$  is calculated using a moving square window of width  $2L + 1$  (where  $L$  is user-defined) applied over the raster of feature vectors  $v(x, y)$ . Consider a focal pixel  $(x_c, y_c)$  having a single feature (a component of a feature vector), for example, slope  $s(x_c, y_c)$ . For every pixel in the window, we calculate a separation vector  $\mathbf{d}_i = (x_i - x_c, y_i - y_c)$ . From the separation vector, we construct a gradient vector

$$\mathbf{g}_i = (s(x_i, y_i) - s(x_c, y_c)) \times \frac{\mathbf{d}_i}{\|\mathbf{d}_i\|} \quad (1)$$

and we use gradient vectors calculated for all pixels in the window to calculate the homogeneity measure  $H$

$$H = \left\| \sum_{i=1}^{(2L+1)^2} \mathbf{g}_i \right\|. \quad (2)$$

A pixel located in a region that is homogeneous with respect to  $s$  has a small value of  $H$ . On the other hand, a pixel located near a boundary between two regions characterized by different values of  $s$  has a large value of  $H$ . A raster constructed by calculating the values of  $H$  for all pixels in the landscape can be interpreted as a grayscale image and is referred to as the  $H$ -image. We denote the  $H$ -image by  $H$ . White areas on  $H$  represent boundaries of homogeneous regions, whereas the dark areas represent the actual regions. The extension of the  $H$ -image concept to encapsulation of gradients in a field of multidimensional feature vectors is straightforward. In order to calculate  $H$  for our 3-D feature vectors  $v(x, y)$ , we calculate the three individual  $H$  values separately for each pixel and combine them to obtain the overall value of  $H$  at that pixel

$$H = \sqrt{w_s H_s^2 + w_\kappa H_\kappa^2 + w_f H_f^2} \quad (3)$$

where  $w_s$ ,  $w_\kappa$ , and  $w_f$  are weights introduced to offset different numerical ranges of the attributes. An example of the  $H$ -image is shown in Fig. 2(a). The watershed transform of  $H$  results in an over segmentation of the  $H$ -image (and, thus, the landscape), an undesirable feature in computer vision, but a desirable feature in the context of segmentation-based classification.

#### B. $K$ -Means-Based Segmentation

Our second approach to segmenting a landscape is agglomerative and incorporates a contiguity-enhanced variant of the standard  $K$ -means clustering algorithm [43], which uses—in addition to terrain attributes—spatial coordinates of pixels as features. In this approach, the pixel-based feature vector is given as  $v = (s, \kappa, f, x, y)$ . The additional spatial features

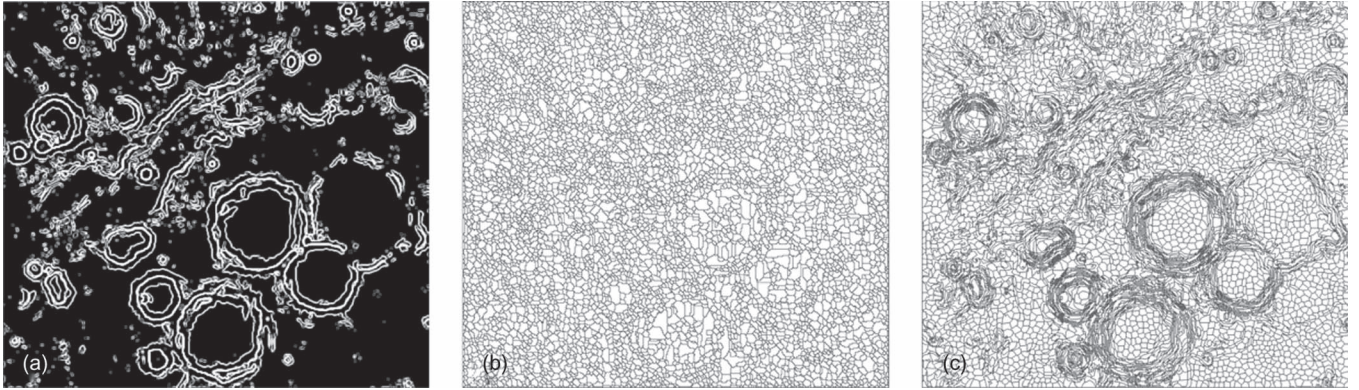


Fig. 2. Tisia site segmentation. (a)  $H$ -image used for watershed-based segmentation. (b) Watershed-based segmentation. (c)  $K$ -means-based segmentation.

( $x$  and  $y$ ) control the size of the segments while providing the resultant segments with very desirable geometric properties. For example, in areas where terrain features are approximately uniform, the local gradient of  $v$  is dominated by changes in  $x$  and  $y$ , leading to the formation of round-shaped segments. On the other hand, in areas where change of terrain features dominates the local gradient of  $v$ , segments tend to exhibit an elongated shape in the direction perpendicular to the gradient of the terrain-only subvector. These properties constitute additional knowledge that could be exploited by the classification module.

The actual segmentation invokes a simple  $K$ -means algorithm [33] applied to spatially enriched pixel-based feature vectors. The size of the segments is controlled by the value of  $k$  (which needs to be large to achieve oversegmentation). The resulting  $k$  clusters do not correspond to  $k$  single-connected spatial segments; instead, each cluster may contain a number of segments. To derive the final segmentation (with  $K > k$  segments), we assign a unique segment identifier to each subset of a cluster corresponding to a single spatially connected region.

### C. Comparing Segmentation Results

We compare the two approaches to scene segmentation on the Tisia site. The watershed-based algorithm with  $L = 1$  produced 7708 segments with sizes ranging from 1 to 267 pixels. The mean segment size is 26 pixels, and the standard variation of segment size is 22 pixels. In the  $k$ -means-based algorithm, we set  $k = 5000$ , resulting in 6593 single-connected segments having sizes ranging from 4 to 117 pixels. The mean segment size is 25 pixels, and the standard variation of segment size is 16 pixels. Fig. 2(b) and (c) shows the resultant segmentations. Notice the different character of the two kinds of segmentation with only the  $K$ -means-based segmentation reflecting closely the site's topography (compare to Fig. 1).

In order to quantitatively compare the two segmentations, we use compactness and isolation [43], two internal measures of clusters quality. Before we explain these measures, we describe our notation.  $K$  stands for the total number of segments, with  $j$  being the segment index ( $j = 1, \dots, K$ );  $v_i$  is a pixel-based feature vector in a segment with  $i$  being the pixel index;  $I_j$  is the set of pixels in segment  $j$ , with  $n_j$  being the size of that set;  $N = \sum_j n_j$  is the total number of pixels in the site,

and  $c_j = (\sum_{i \in I_j} v_i) / n_j$  is the mean feature vector in segment  $j$ ;  $c = (\sum_j n_j c_j) / N$  is the mean feature vector calculated over all pixels in the site.

In calculating compactness and isolation, we use only the nonspatial part of the pixel-based feature vectors,  $v = \{s, \kappa, f\}(x, y)$ . The compactness  $V_j$  of a single segment is defined as the within-segment variance of its feature vectors

$$V_j = \frac{1}{n_j} \sum_{i \in I_j} (v_i - c_j)^2. \quad (4)$$

On each segment, we expect all feature vectors to be nearly identical, so that small values of  $V_j$  are desirable. We calculate compactness of the entire segmentation as a weighted average (based on size) of each individual segment compactness

$$V = \frac{1}{N} \sum_{j=1}^K n_j V_j. \quad (5)$$

A normalized version of  $V$  is obtained by dividing over the variance of the pixel-based feature vectors on the entire site

$$V_0 = \left( \sum_{i=1}^N (v_i - c)^2 \right) / N. \quad (6)$$

Our final measure of segmentation compactness is defined as follows:

$$V_* = V / V_0. \quad (7)$$

A segmentation with a smaller value of  $V_*$  is better inasmuch as it has segments that, on average, are more uniform.

The isolation  $S_j$  of a single segment is defined as the ratio of the feature-based distance between this segment and its closest neighbor, and the segment's feature-based size

$$S_j = \sqrt{\frac{\min_l (c_l - c_j)^2}{\left( \sum_{i \in I_j} (v_i - c_j)^2 \right) / n_j}} \quad (8)$$

where  $l$  indexes the neighbors of segment  $j$ . A large value indicates that the difference between a segment and its closest neighbor is significantly larger than the differences between individual pixels within the segment. Such segment is well isolated from its neighbors. We calculate the isolation of the

entire segmentation as a weighted average (based on size) of each individual segments' isolation

$$S = \frac{1}{N} \sum_{j=1}^K n_j S_j. \quad (9)$$

A segmentation with a larger value of  $S$  is better inasmuch as it has segments that, on average, are more isolated from their neighbors. For the watershed-based segmentation of the Tisia site [Fig. 2(b)],  $V_* = 0.068$  and  $S = 0.061$ , whereas for the  $K$ -means-based segmentation of the same site [Fig. 2(c)],  $V_* = 0.022$  and  $S = 0.087$ . These results indicate that  $K$ -means-based segmentation is of significantly higher quality than the watershed-based segmentation. In addition, the  $K$ -means-based segmentation has a preferable (flatter) distribution of segment sizes. Overall, the  $K$ -means-based segmentation shows better performance with the only disadvantage of having higher computational cost.<sup>1</sup>

#### IV. CLASSIFICATION

The classification module assigns a label (landform designation) to unlabeled segments based on patterns learned from examples. In our framework, the subjects of classification are segment-based feature vectors associated with individual segments. It is important to stress that these segment-based feature vectors are not the same as the pixel-based feature vectors used for segmentation. First, the location information, contained in spatial coordinates for the  $K$ -means-based segmentation, is no longer necessary or desirable in the segment-based vectors; the landform designation should not depend on a specific location of a landscape element. The major components of the segment-based features are terrain parameters averaged over an ensemble of member pixels (i.e., vectors  $c_j$ ). Additional segment-based features are calculated from the shape of the segments and properties of neighboring segments. The spatial features describe the segment itself (i.e., its geometrical and neighboring properties).

##### A. Segment-Based Features

Each segment is represented by a combination of physical and spatial features. Physical features comprise segmentation features averaged over the constituent pixels of the segments; they are derived from components of the vector  $c_j$ :  $\bar{s}_j$ ,  $\bar{\kappa}_j$ , and  $\bar{f}_j$ , where the bar indicates averages over the segment's constituent pixels.

Spatial features are obtained using the segment's shape measure and the neighborhood context measure. The shape measure is computed in terms of the shape complexity index (SCI) [16] for each segment as follows:

$$SCI = \frac{P}{2\pi r} \quad r = \sqrt{\frac{A}{\pi}} \quad (10)$$

<sup>1</sup>In the computer vision community,  $K$ -means is generally perceived to be faster and more efficient than state-of-the-art segmentation routines. However, this is only true for small values of  $k$ . In our application where  $k \sim 10^3 - 10^4$ ,  $k$ -means turns out to be computationally expensive.

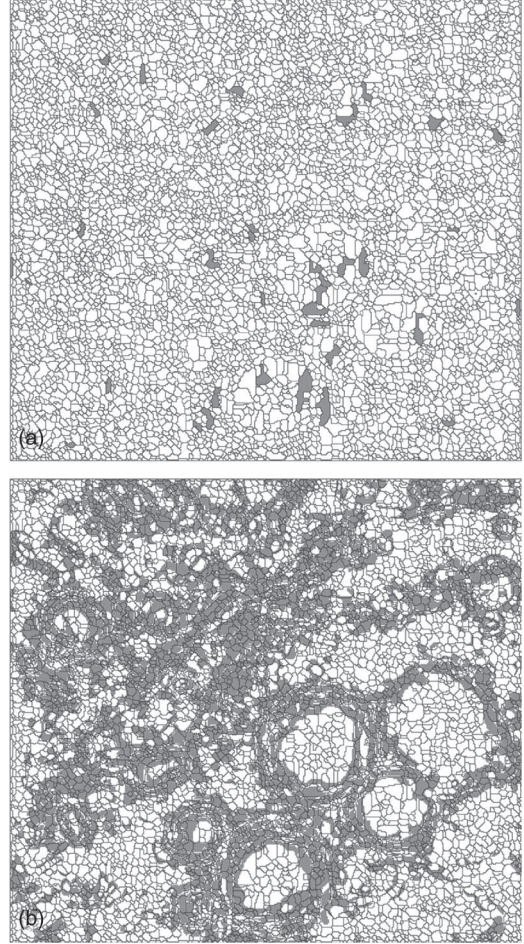


Fig. 3. Comparison of segments elongation in the Tisia site. Gray-colored segments indicate elongated segments with  $SCI \geq 1.75$ . (a) Watershed-based segmentation. (b)  $K$ -means-based segmentation.

where  $P$  is the perimeter of the segment's boundary,  $A$  is the area of the segment, and  $r$  is the radius of a circle with the same surface area as the segment. SCI is a measure of segment circularity. The closer the value of SCI to 1.0, the more circular the object; on the other hand, thin ringlike shapes tend to have SCI values of 2.5 and higher. The perimeter  $P$  and area  $A$  of the segments are calculated using Minkowski functionals [26].

We expect that the SCI to be a valuable feature for landform identification. Note that this feature is only available in the segmentation-based classification approach and not available in the standard pixel-based classification approach. In order to investigate the importance of the SCI in delineating landforms, we have produce a binary image  $B_{SCI}$  for the Tisia site, according to the following transformation:

$$B_{SCI}(j) = \begin{cases} B_{SCI}(j) = 1, & \text{for } SCI(j) \geq SCI_{th} \\ B_{SCI}(j) = 0, & \text{for } SCI(j) < SCI_{th} \end{cases} \quad (11)$$

where  $j = 1, \dots, K$  indexes the segments and  $SCI_{th}$  is a threshold value that decides when segments are considered elongated. Fig. 3(a) and (b) shows the images  $B_{SCI}$  for the watershed-based and the  $k$ -means-based segmentations of the

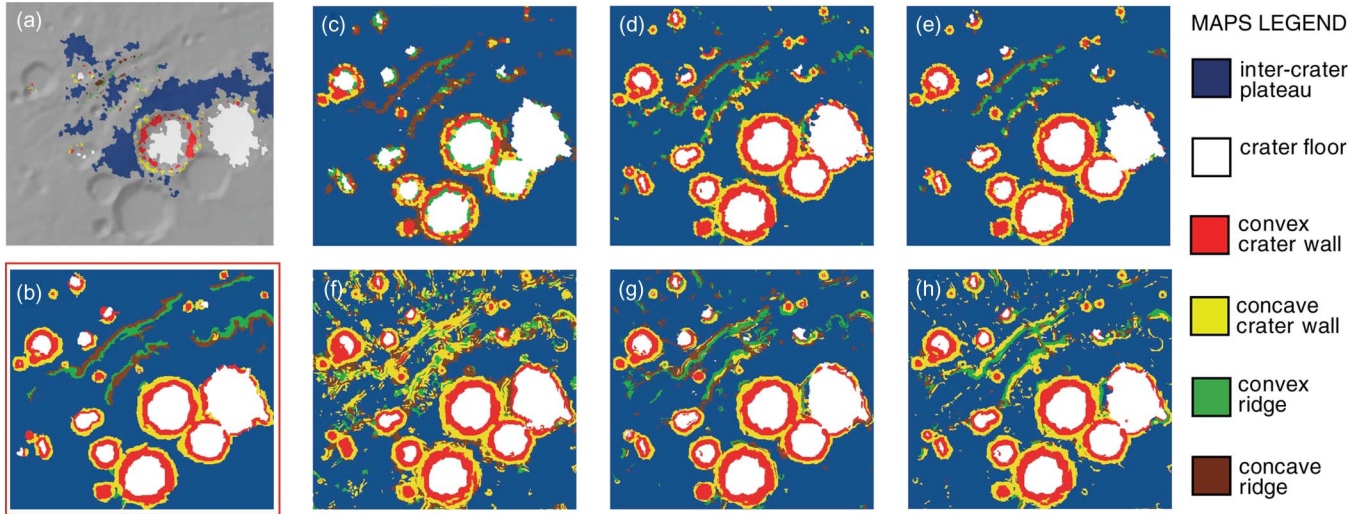


Fig. 4. Geomorphic maps of the Tisia site generated by different segmentation/classification methods. (a) Labeled regions; different landform classes are coded by different colors as given by the legend. Unlabeled regions are displayed in gray. (b) Analyst-drawn map (“ground truth”). Maps based on the watershed segmentation [(c)—Naive Bayes, (d)—Bagging, (e)—SVM]. Maps based on the  $K$ -means segmentation [(f)—Naive Bayes, (g)—Bagging, (h)—SVM] (for interpretation of the references to colors in this figure, the reader is referred to the web version of this paper).

Tisia site using  $SCI_{th} = 1.75$ . There is a striking difference between the two images. Whereas, in the  $K$ -means-based segmentation, the segments corresponding to ridges and crater walls are elongated and have  $SCI > SCI_{th}$ , no such pattern is observed in the watershed-based segmentation, indicating that most watershed-derived segments are fairly circular. This difference stems from the way the two algorithms define segments. In the watershed algorithm, segments are defined by the smallest “depressions” in the  $H$ -image, essentially by the noise in the  $H$ -image, which leads to relatively circular shapes. On the other hand, the contiguity-enhanced  $K$ -means algorithm is particularly designed (see Section III-B) to produce segments with shapes that reflect gradients of physical features. Thus,  $SCI$  is helpful in distinguishing landforms only when used in conjunction with the  $K$ -means-based segmentation.

As aforementioned in Section I-C, the automatic classification of landforms is challenging because different landforms may be characterized by very similar terrain attributes but different spatial context. For instance, segments making up craters’ walls and segments constituting ridges not associated with craters may have similar values of slope, curvature, and flood but located in different spatial contexts. Our method takes into consideration spatial context by means of neighborhood context measures. Ideally, we would like to know classes of segment’s neighbors to establish its spatial context, but such information is not available prior to classification. However, even for unlabeled segments, a preliminary categorization of segments into low-, medium-, and high-slope categories is possible on the basis of statistics of the values of  $\bar{s}_j$ ,  $j = 1, \dots, K$ . Such categorization is used to calculate the neighborhood property of a segment  $j$ ,  $\{a_1^s, a_2^s, a_3^s\}_j$ , where  $a_l^s$ ,  $l = 1, 2, 3$ , is the percentage of the segment boundary adjacent to neighbors belonging to slope category  $l$ . Similar neighborhood properties,  $\{a_1^c, a_2^c, a_3^c\}_j$ ,  $\{a_1^f, a_2^f, a_3^f\}_j$ , are calculated on the basis of curvature and flood values, yielding a total of nine features corresponding to the spatial context of a given segment. Segment-based feature vectors, denoted by

TABLE I  
NUMBER OF LABELED SEGMENTS PER CLASS

Segmentation	Classes						Labeled	Total
	1	2	3	4	5	6		
watershed	788	291	156	156	57	50	1498	7708
$K$ -means	345	243	126	67	18	30	829	6593

$u$ , are defined as follows when  $k$ -means-based segmentation is used:

$$u = \left\{ \bar{s}, \bar{\kappa}, \bar{f}, SCI, a_1^s, a_2^s, a_3^s, a_1^c, a_2^c, a_3^c, a_1^f, a_2^f, a_3^f \right\}. \quad (12)$$

The definition is slightly modified when watershed-based segmentation is used by removing the  $SCI$  component.

### B. Labeled Training Set

The labeled (training) set of segments was generated by manually labeling 30% (by surface area) of the Tisia site into six classes corresponding to six landforms, as described in Section II: intercrater plateau (class 1), crater floors (class 2), convex crater walls (class 3), concave crater walls (class 4), convex ridges (class 5), and concave ridges (class 6). Fig. 4(a) shows the labeled part of the Tisia site. Depending on the segmentation used, the labeled area results in a different number of labeled segments. Table I provides details on the number of labeled segments.

### C. Classifiers

We applied different learning algorithms in our test sites for segment classification and to generate geomorphic maps. First, we tried a simple classifier as a baseline for comparison to determine if a limited family of models could perform satisfactorily in our particular domain. Naive Bayes belongs to the class of generative Bayesian classifiers that estimate the posterior probability of the class label given a feature vector

TABLE II  
 ACCURACY FOR THE THREE CLASSIFIERS AND TWO SEGMENTATIONS TECHNIQUES (STANDARD DEVIATIONS ARE GIVEN IN PARENTHESES).  
 AN ASTERISK ON AN ENTRY REPRESENTS STATISTICALLY SIGNIFICANT IMPROVEMENT OVER THE NAIVE BAYES CLASSIFIER  
 (AT 95% CONFIDENCE LIMITS USING A T-STUDENT DISTRIBUTION)

Dataset	Naive Bayes	Bagging with C4.5	SVM (quadratic kernel)
<i>K</i> -means	88.65(3.17)	90.95(2.57)*	91.06(2.50)*
watershed	85.27(2.51)	90.28(1.95)*	91.30(1.58)*

representing the instance (segment) using Bayes’ theorem [19]. The computation of the likelihood is simplified by assuming feature independence given the class label. The independence assumption is false in our case as all the features are derived from a single source of information—the site’s DEM.

Our second classifier imposes a flexible model over the feature space and was used to test the importance of reducing bias by employing a rich family of models. Support-vector machines (SVMs) is a statistical learning algorithm that works by finding an optimal hyperplane in a (transformed) feature space [6]. The optimal hyperplane maximizes the separation between classes. SVM exploits local data patterns and has been found to be effective in spatial data-mining applications [36].

We finally employed a classifier that reduces variance through model combination. The goal was to explore the importance of reducing generalization error incurred through model variability. Bagging is an ensemble learning algorithm [7], [12]; it generates multiple models by running a single learning algorithm multiple times over bootstrapped samples of the training set. The final class label is the result of voting over the contributing models (one from each bootstrap sample). Bagging is known to work well for complex data sets and is particularly attractive when the training set is noisy [12] as is the case in our application. We use a decision tree (C4.5) as the base learner.

We employed the algorithms earlier as implemented in the software package WEKA [49]. We used default parameters because our empirical assessment serves simply to illustrate the potential application of this framework. Nevertheless, we performed a parameter search over the Gaussian, linear, quadratic, and cubic kernels in the case of SVMs at different values of the slack variable. The best results were obtained using a quadratic kernel with the slack value ranging between  $C = 1$  and 2.

Accuracy of the three classifiers described earlier was computed using ten runs of tenfold cross-validation on the Tisia site training set (see Section IV-B). Accuracy is the percentage of pixels that are labeled in agreement with the analyst-drawn map. Results are shown in Table II. Both Bagging with C4.5 and SVM show significant improvement in accuracy as compared with Naive Bayes, which points to the importance of imposing a rich family of models by the classifier in our domain. There is no significant difference in performance between Bagging and SVM.

## V. RESULTS

The segmentation-based classification technique described in Sections III and IV was applied to six sites on Mars. For each site, we have calculated the watershed-based and the *K*-means-based segmentations. Each segmentation solution was classified

using three learning algorithms (Naive Bayes, Bagging with C4.5, and SVM) trained using the same labeled training set (a subset of Tisia site) described in Section IV-B.

### A. Tisia Site

For our primary test site (Tisia), we have generated six maps shown in Fig. 4(c)–(e) and (f)–(h). Fig. 4(b) shows the hand-labeled “ground-truth” map of Tisia. This is how a typical domain expert would map the six landforms in this site. A human-produced map does not really constitute a ground truth because an analyst is likely to draw an idealized map that misses details and projects a human conceptualization of the entire landscape, even if it contradicts local measurements. Maps based on the watershed segmentation [Fig. 4(c)–(e)] have a “simple” look as they lack small-scale details, whereas maps based on the *K*-means segmentation [Fig. 4(f)–(h)] look “busy” as they exhibit more small-scale details. On the basis of a casual visual inspection, one could conclude that maps based on watershed segmentation look more like the analyst-drawn map [Fig. 4(b)] than the maps based on *K*-means segmentation; this is despite the higher quality of *K*-means segmentation (Section III-C) and the fact that segment-based feature vectors used to classify *K*-means-generated segments carry relevant information. However, closer inspection of the generated maps shows that maps based on *K*-means segmentation correctly reflect some small-scale details that are absent from the watershed segmentation and the analyst-drawn map. Overall, maps generated by Naive Bayes are inaccurate and inferior to maps generated by Bagging and SVM. Maps generated by Bagging and SVM have different character; the SVM-generated map shows more detail, whereas the Bagging-generated map shows better discrimination between crater walls and ridges.

Detailed information about the six maps calculated for the Tisia test site are given in Table III. The two horizontal sections of this table report on results obtained using the watershed-based segmentation and the *K*-means-based segmentation. Each section has six subsections. The first subsection gives the names of the landforms. The second subsection gives the number of segments in each landform class. The remaining four subsections report on average values of different terrain parameters in all six landform classes. These values are normalized (a class with highest value receives a score of 100). For example, in a map produced by SVM on the basis of the watershed segmentation, the convex-crater-wall class is characterized by the highest values of slope (a score of 100). The slopes in the concave-crater-wall class are, on average, only 80% as steep (score 80). The convex- and concave-ridge classes are both, on average, 41% as steep. The plateau class is 3%, and the crater-floor class is the least steep; on average, only 1% as

TABLE III  
 PROPERTIES OF TOPOGRAPHIC LANDFORM CLASSES AS GIVEN BY DIFFERENT CLASSIFIERS APPLIED TO THE TISIA SITE. FOR EACH CLASSIFICATION SOLUTION (MAP) AND TERRAIN ATTRIBUTE, A COLUMN GIVES AVERAGE MAGNITUDE OF THIS ATTRIBUTE IN A GIVEN CLASS (RANGING FROM  $\pm 100$  TO 0). **NB**—NAIVE BAYES, **B**—BAGGING WITH C4.5, **SVM**—SUPPORT VECTOR MACHINES

watershed based segmentation															
class	segments			area			slope			curvature			flood		
	NB	B	SVM	NB	B	SVM	NB	B	SVM	NB	B	SVM	NB	B	SVM
plateau	5588	5354	5809	100	100	100	1	3	3	-1	-1	-1	1	2	3
floor	569	464	476	15	14	15	1	1	1	10	6	6	100	100	100
cvx. wall	384	687	573	3	10	9	100	100	100	79	66	68	92	92	94
con. wall	324	675	572	4	10	8	83	79	80	-84	-100	-100	38	7	11
cvx. ridge	210	258	136	1	1	1	46	35	41	100	46	54	79	2	6
con. ridge	616	270	142	7	1	2	36	40	41	-70	-35	-49	1	1	1
<i>K</i> -means based segmentation															
class	segments			area			slope			curvature			flood		
	NB	B	SVM	NB	B	SVM	NB	B	SVM	NB	B	SVM	NB	B	SVM
plateau	2660	3811	3613	100	100	100	3	1	3	-1	-1	1	1	1	2
floor	463	614	519	14	15	15	1	1	1	7	6	3	100	100	100
cvx. wall	793	739	754	13	9	11	100	100	100	100	52	82	97	91	95
con. wall	1846	739	1305	30	7	18	58	70	62	-70	-100	-100	8	4	8
cvx. ridge	238	272	254	1	1	1	20	25	36	10	43	55	7	8	7
con. ridge	593	355	148	11	2	1	23	29	31	-5	-16	-2	1	1	1

TABLE IV  
 PERFORMANCE MEASUREMENTS FOR MAPS OF THE TISIA SITE GENERATED BY DIFFERENT CLASSIFIERS. THE ENTRIES FOR INDIVIDUAL LANDFORMS ARE (PRECISION/RECALL). **NB**—NAIVE BAYES, **B**—BAGGING WITH C4.5, **SVM**—SUPPORT VECTOR MACHINES

watershed based segmentation							
classifier	overall accuracy	plateau	floor	cvx. wall	con. wall	cvx. ridge	con. ridge
<b>NB</b>	84.67	0.94 / 0.97	0.93 / 0.93	0.87 / 0.39	0.57 / 0.37	0.12 / 0.12	0.20 / 0.51
<b>B</b>	89.31	0.95 / 0.96	0.97 / 0.87	0.80 / 0.83	0.65 / 0.75	0.51 / 0.45	0.38 / 0.37
<b>SVM</b>	89.71	0.92 / 0.98	0.96 / 0.90	0.87 / 0.75	0.72 / 0.70	0.62 / 0.29	0.48 / 0.29
<i>K</i> -means based segmentation							
classifier	overall accuracy	plateau	floor	cvx. wall	con. wall	cvx. ridge	con. ridge
<b>NB</b>	74.11	0.99 / 0.76	0.99 / 0.80	0.70 / 0.78	0.32 / 0.83	0.14 / 0.19	0.08 / 0.25
<b>B</b>	87.42	0.96 / 0.92	0.94 / 0.92	0.80 / 0.85	0.67 / 0.72	0.34 / 0.47	0.25 / 0.40
<b>SVM</b>	86.10	0.97 / 0.91	0.98 / 0.87	0.77 / 0.79	0.46 / 0.83	0.46 / 0.54	0.18 / 0.12

steep as the convex-crater-wall class. For the curvature attribute, positive values refer to convex regions, while negative values refer to concave regions.

Table IV gives accuracy rates for maps of the Tisia site. Disregarding maps produced by Naive Bayes, accuracy rates are above 86%. Note that maps based on the watershed segmentation have slightly higher rates than maps based on the *K*-means segmentation. This reflects the watershed segmentation's simpler character, more in line with the analyst drawing. The table also shows precision and recall rates for six landform classes. Results show that intercrater-plateau, crater-floor, and convex-crater-wall landforms are designated with high accuracy. Concave crater walls are detected with less accuracy, and ridges are essentially difficult to identify correctly. This is because local ridges look like crater walls, even though they are different landforms in the context of the entire landscape.

### B. Other Sites

The remaining five test sites, Vichada, Al-Qahira, Dawes, Evros, and Margaritifer, represent the same type of Martian surface as the Tisia site. The same six landform classes are present; one would then expect that models generated from the Tisia site would be able to map these sites accurately. In general,

maps of these sites have the same relative character as maps from the Tisia site. Fig. 5 shows a sample of the results. The top row in this figure shows the topography of each site. The topography helps to visualize the landscape and serves as a guide for a visual assessment of map quality. The middle row shows maps generated by the SVM classifier applied to the watershed segmentation, and the bottom row shows maps generated by the SVM classifier applied to the *K*-means segmentation. As in the case of the Tisia site, maps originating from the watershed segmentation lack small-scale details, whereas maps originating from the *K*-means segmentation show more details but tend to generate more misclassifications.

The Vichada site was hand labeled by an analyst. Table V shows accuracy performance for maps of this site. Maps corresponding to watershed segmentation have accuracy rates only slightly lower than those of the Tisia site. However, these maps are much less useful than Tisia because they miss most ridges. The Vichada site is dominated by the plateau class, identified correctly during prediction (which explains the high accuracy rates). One gains more insight when evaluating precision/recall rates for individual landforms; such evaluation shows poor performance on all classes except the plateau class. Maps originating from the *K*-means segmentation have precision/recall rates similar to those recorded for the Tisia site.

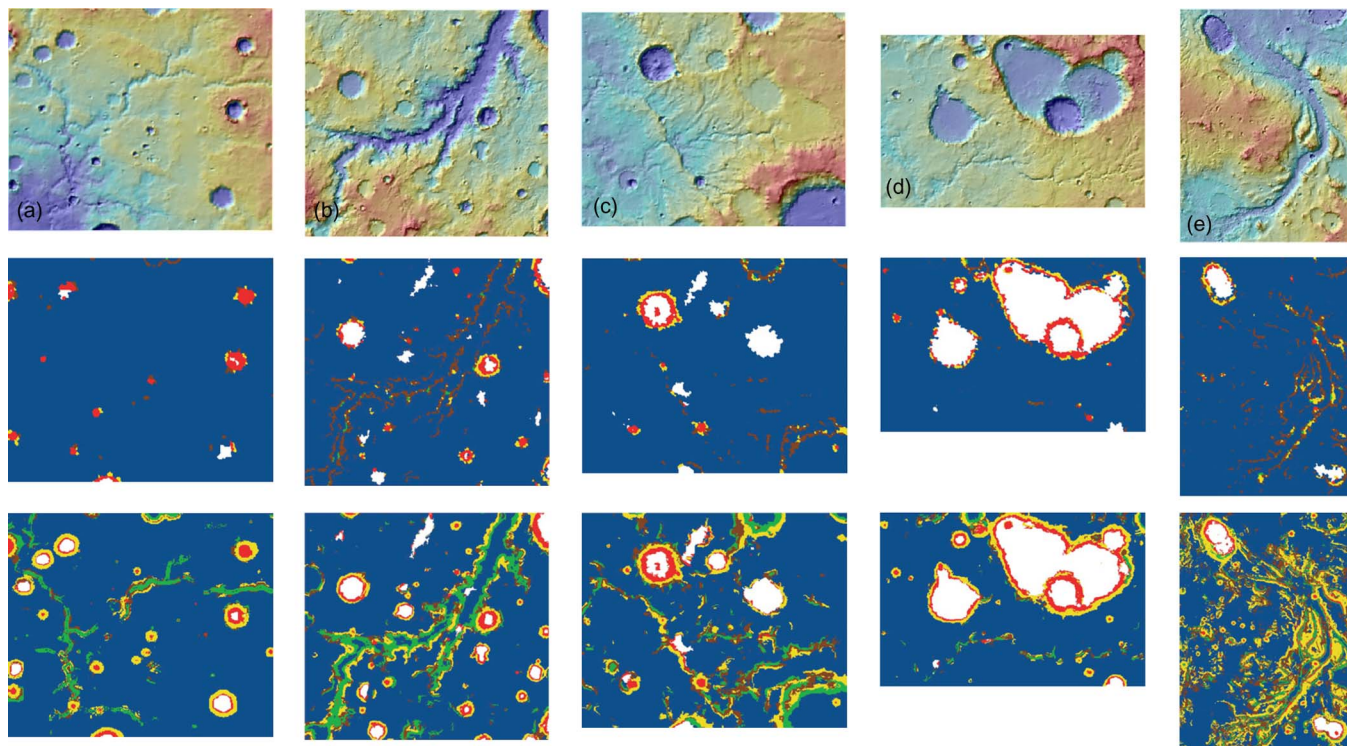


Fig. 5. Automatically generated six-landform geomorphic maps of (a) Vichada, (b) Al-Qahira, (c) Dawes, (d) Evros, and (e) Margaritifer sites using the SVM classifier. The top row shows sites' topography, the middle row shows maps originating from the watershed segmentation, and the bottom row shows the maps originating from the  $K$ -means segmentation. For the map legend, see Fig. 4 (for interpretation of the references to colors in this figure, the reader is referred to the web version of this paper).

TABLE V  
ACCURACY OF MAPPING INDIVIDUAL LANDFORMS IN THE VICHADA SITE USING DIFFERENT CLASSIFIERS. THE ENTRIES FOR LANDFORMS ARE (PRECISION/RECALL). **NB**—NAIVE BAYES, **B**—BAGGING WITH C4.5, **SVM**—SUPPORT VECTOR MACHINES

watershed based segmentation							
classifier	overall accuracy	plateau	floor	cvx. wall	con. wall	cvx. ridge	con. ridge
<b>NB</b>	83.05	0.86 / 0.99	0.40 / 0.30	0.73 / 0.21	0.41 / 0.06	0.001 / 0.0003	0.025 / 0.007
<b>B</b>	85.03	0.87 / 0.99	0.49 / 0.25	0.66 / 0.60	0.60 / 0.31	0.35 / 0.03	0.07 / 0.003
<b>SVM</b>	83.79	0.85 / 0.99	0.44 / 0.23	0.66 / 0.37	0.87 / 0.07	0.0 / 0.0	0.02 / 0.002
$K$ -means based segmentation							
classifier	overall accuracy	plateau	floor	cvx. wall	con. wall	cvx. ridge	con. ridge
<b>NB</b>	39.60	0.97 / 0.36	0.0 / 0.0	0.62 / 0.73	0.31 / 0.09	0.81 / 0.11	0.67 / 0.25
<b>B</b>	69.20	0.94 / 0.75	0.71 / 0.78	0.54 / 0.69	0.73 / 0.46	0.10 / 0.84	0.09 / 0.008
<b>SVM</b>	86.00	0.92 / 0.95	0.60 / 0.82	0.80 / 0.44	0.60 / 0.66	0.41 / 0.56	0.25 / 0.08

## VI. SUMMARY AND CONCLUSION

In this paper, we have proposed a machine-learning-based method for annotating planetary surfaces with geomorphic labels (i.e., for machine generation of geomorphic maps). This is a challenging problem for the following reasons. First, landscapes are more difficult to label than multispectral images because their characterization is based on fewer features. A multispectral image has at least six channels (colors), whereas landform characterization tends to be limited (this paper derives three topographic features). Second, space-related data exhibit less quality than terrestrial data. A Martian DEM is much coarser and noisier than terrestrial DEMs. High-quality DEMs facilitate extraction of additional features (such as several types of surface curvature). Moreover, terrestrial topographic data can often be supplemented by other data sets, such as, for example,

hydrological data. Such additional data sets are not available in space applications. Developing an application for mapping planetary surfaces, therefore, presents challenges not found in the terrestrial domain. Our approach is based on a segmentation step preceding classification; this is because segments offer the opportunity to create additional features, taking into account spatial context (albeit only local context). This paper is intended to serve as a guideline for future work related to automated planetary mapping. It is important to add that the particular landform classes presented in this paper are examples of geomorphic studies of cratered terrain on planet Mars. In order to apply our framework to generate maps of different landforms of interest on Mars, Earth, or other planets, different classes must be identified by a domain expert (resulting in different training sets).

As a result of our assessment of different segmentation and classification algorithms, we offer the following design choices for future machine-mapping applications. For a rough map that needs to be generated rather quickly, a combination of watershed-based segmentation with either Bagging or SVM is preferable. An application based on such a combination may be useful in cases where maps need to be generated on-board a spacecraft. For a more detailed map, a combination of  $K$ -means-based segmentation with either Bagging or SVM is recommended. Since the  $K$ -means segmentation is slow, applications based on such a combination may be more appropriate for an offline analysis. Bagging is more sensitive to small local changes in topographic data and is preferable in applications where high sensitivity is desired; an example is found in maps designed to detect valley networks on Mars. SVM is less sensitive to small changes in topography and produces smoother maps (this is not so evident on the Tisia site but quite evident on maps from other sites). SVM is preferable in applications where smoother maps are desirable.

This paper also shows the necessity of using a representative training set. Our six test sites are from roughly similar terrains (same geological unit); one would expect that our training set, extracted from a single site, should yield similar results on other sites. This was not the case. A comparison of Tables IV and V indicates that the Tisia site was mapped with higher accuracy than the Vichada site. In addition, visual inspection of Fig. 5 shows that the Margaritifer site is poorly mapped, even though it bears topographic similarity to the Al-Qahira site (the former resulting in a good map). Although different sites may have similar landforms, particular characterizations may exhibit different ranges of terrain parameters. As an example, ridges in Al-Qahira and Margaritifer sites look similar, but exhibit different slope magnitudes. Hence, in future applications, we advocate flagging segments labeled with low confidence for additional manual labeling.

We envision two types of spin-off applications. First is an offline automated data-analysis module. Frequently, geological analysis consists of a descriptive comparison among maps (of two or more sites) in order to identify similarities and/or differences in the presence and character of selected landforms. Because our methodology produces digital thematic maps of landforms, such maps can be subjected to machine-assisted comparison (see, for example, [31] and [32]). Second is an onboard application that generates geomorphic maps for the purpose of data compression. Such maps can be cheaply transmitted to Earth to assist ground controllers in decision making. Future work will address faster algorithms for quality segmentation (to replace the slow  $K$ -means algorithm), development of additional topography-derived features, incorporating imagery data to add texture information, and a robust approach to incorporate context information (e.g., using Markov random fields).

#### ACKNOWLEDGMENT

A portion of this paper was conducted at the Lunar and Planetary Institute, which is operated by the Universities Space Research Association under Contract CAN-NCC5-679 with the National Aeronautics and Space Administration. This is Lunar and Planetary Institute Contribution No. 1433.

#### REFERENCES

- [1] R. Adams and L. Bischof, "Seeded region growing," *IEEE Trans. Pattern Anal. Mach. Intell.*, vol. 16, no. 6, pp. 641–647, Jun. 1994.
- [2] L. Bandeira, J. Saraiva, and P. Pina, "Impact crater recognition on Mars based on a probability volume created by template matching," *IEEE Trans. Geosci. Remote Sens.*, vol. 45, no. 12, pp. 4008–4015, Dec. 2007.
- [3] T. Barata, E. I. Alves, J. Saraiva, and P. Pina, "Automatic recognition of impact craters on the surface of Mars," in *Proc. Image Anal. Recog.*, Berlin, Germany: Springer-Verlag, 2004, vol. 3212, pp. 489–496.
- [4] S. Belongie, C. Carson, H. Greenspan, and J. Malik, "Color- and texture-based image segmentation using EM and its application to content-based image retrieval," in *Proc. 6th Int. Conf. Comput. Vis.*, 1998, pp. 675–682.
- [5] S. Beucher, "The watershed transformation applied to image segmentation," *Scanning Microsc. Int.*, no. 6, pp. 299–314, 1992.
- [6] B. E. Boser, I. Guyon, and V. Vapnik, "A training algorithm for optimal margin classifiers," in *Proc. Comput. Learn. Theory*, 1992, pp. 144–152.
- [7] L. Breiman, "Bagging predictors," *Mach. Learn.*, vol. 24, no. 2, pp. 123–140, 1996.
- [8] B. D. Bue and T. F. Stepinski, "Machine detection of Martian impact craters from digital topography data," *IEEE Trans. Geosci. Remote Sens.*, vol. 45, no. 1, pp. 265–274, Jan. 2007.
- [9] M. C. Burl, T. Stough, W. Colwell, E. B. Bierhaus, W. J. Merline, and C. Chapman, "Automated detection of craters and other geological features," presented at the 6th Int. Symp. Artif. Intell., Robot. Autom. Space, Montreal, QC, Canada, Jun. 2001, Paper 01-1008.
- [10] Y. Cheng, A. E. Johnson, L. H. Matthies, and C. F. Olson, "Optical landmark detection for spacecraft navigation," presented at the AAS/AIAA Astrodyn. Spec. Conf., Ponce, Puerto Rico, Feb. 2003.
- [11] Y. Deng and B. S. Manjunath, "Unsupervised segmentation of color-texture regions in images and video," *IEEE Trans. Pattern Anal. Mach. Intell.*, vol. 23, no. 8, pp. 800–810, Aug. 2001.
- [12] T. G. Dietterich, "Ensemble methods in machine learning," in *Proc. 1st Int. Workshop Multiple Classifier Syst.*, 2000, vol. 1857, pp. 1–15.
- [13] L. Dragut and T. Blaschke, "Automated classification of landform elements using object-based image analysis," *Geomorphology*, vol. 81, no. 3/4, pp. 330–344, Nov. 2006.
- [14] H. Feng, D. A. Castanon, and W. C. Karl, "A curve evolution approach for image segmentation using adaptive flows," in *Proc. Int. Conf. Comput. Vis.*, 2001, vol. 2, pp. 494–499.
- [15] A. L. Gallant, D. D. Brown, and R. M. Hoffer, "Automated mapping of Hammond's landforms," *IEEE Geosci. Remote Sens. Lett.*, vol. 2, no. 4, pp. 384–388, Oct. 2005.
- [16] T. Hengl, "Pedometric mapping: Bridging the gaps between conventional and pedometric approaches," Ph.D. dissertation, Wageningen Univ., Wageningen, The Netherlands, 2003.
- [17] R. Honda, Y. Iijima, and O. Konishi, "Mining of topographic feature from heterogeneous imagery and its application to lunar craters," in *Progress in Discovery Science, Final Report of the Japanese Discovery Science Project*. London, U.K.: Springer-Verlag, 2002, pp. 395–407.
- [18] F. Jing, M. Li, H. Zhang, and B. Zhang, "Unsupervised image segmentation using local homogeneity analysis," in *Proc. IEEE Int. Symp. Circuits Syst.*, 2003, pp. II-456–II-459.
- [19] G. H. John and P. Langley, "Estimating continuous distributions in Bayesian classifiers," in *Proc. 11th Conf. Uncertainty Artif. Intell.*, San Mateo, CA, 1995, pp. 338–345.
- [20] J. John, H. Lowry, R. Ramsey, K. Boykin, D. Bradford, P. Comer, S. Falzarano, W. K. J. Kirby, L. Langa, J. Prior-Magee, G. Manis, L. O'Brien, K. Pohs, W. Rieth, T. Sajwaj, S. Schrader, K. A. Thomas, D. S. K. Schulz, B. Thompson, C. Wallace, C. Velasquez, E. Waller, and B. Wolk, "The Southwest Regional Gap Analysis Project: Final Report on Landcover Mapping Methods," Utah State Univ., Logan, UT, Oct. 2005. Tech. Rep.
- [21] J. Kim, J. Muller, S. van Gasselt, J. Morley, and G. Neukum, "Automated crater detection, a new tool for Mars cartography and chronology," *Photogramm. Eng. Remote Sens.*, vol. 71, no. 10, pp. 1205–1217, 2005.
- [22] D. Landgrebe, "The evolution of Landsat data analysis," *Photogramm. Eng. Remote Sens.*, vol. 63, no. 7, pp. 859–867, 1997.
- [23] D. Landgrebe, "Information extraction principles and methods for multispectral and hyperspectral image data," in *Information Processing for Remote Sensing*. Singapore: World Scientific, 1999, ch. 1.
- [24] B. Leroy, G. Medioni, E. Johnson, and L. Matthies, "Crater detection for autonomous landing on asteroids," *Image Vis. Comput.*, vol. 19, no. 11, pp. 787–792, 2001.
- [25] R. Martins, P. Pina, J. S. Marques, and M. Silveira, "Crater detection by a boosting approach," *IEEE Geosci. Remote Sens. Lett.*, vol. 6, no. 1, pp. 127–131, Jan. 2009.

- [26] K. Michielsen and H. De Raedt, "Integral-geometry morphological image analysis," *Phys. Rep.*, vol. 347, no. 6, pp. 461–538, 2001.
- [27] G. Miliareis and N. Kokkas, "Segmentation and object-based classification for the extraction of the building class from LIDAR DEMs," *Comput. Geosci.*, vol. 33, no. 8, pp. 1076–1087, 2007.
- [28] H. Mitasova and L. Mitas, "Interpolation by regularized spline with tension: I. Theory and implementation," *Math. Geol.*, vol. 25, no. 6, pp. 641–655, 1993.
- [29] R. Nock and F. Nielsen, "Statistical region merging," *IEEE Trans. Pattern Anal. Mach. Intell.*, vol. 26, no. 11, pp. 1452–1458, Nov. 2004.
- [30] C. Plesko, S. Brumby, E. Asphaug, D. Chamberlain, and T. Engel, "Automatic crater counts on Mars," in *Proc. Lunar Planet. Inst. Conf. Abstr.*, S. Mackwell and E. Stansbery, Eds., 2004, pp. 1935–1936.
- [31] T. K. Remmel and F. Csillag, "Spectra of coincidences between spatial data sets: Toward hierarchical inferential comparisons of categorical maps," in *Proc. GeoComputation Conf.*, 2005.
- [32] T. K. Remmel and F. Csillag, "Mutual information spectra for comparing categorical maps," *Int. J. Remote Sens.*, vol. 27, no. 7, pp. 1425–1452, 2006.
- [33] D. G. S. Richard, O. Duda, and P. E. Hart, *Pattern Classification*, 2nd ed. New York: Wiley, 2000.
- [34] G. Salamunićar and S. Lončarić, "GT-57633 catalogue of Martian impact craters developed for evaluation of crater detection algorithms," *Planet. Space Sci.*, vol. 56, no. 15, pp. 1992–2008, Dec. 2008.
- [35] G. Salamunićar and S. Lončarić, "Open framework for objective evaluation of crater detection algorithms with first test-field subsystem based on MOLA data," *Adv. Space Res.*, vol. 42, no. 1, pp. 6–19, 2008.
- [36] M. Sharifzadeh, C. Shahabi, and C. Knoblock, "Learning approximate thematic maps from labeled geospatial data," presented at the Int. Workshop Next Generation Geospatial Inf., Cambridge, MA, 2003.
- [37] J. Shi and J. Malik, "Normalized cuts and image segmentation," *IEEE Trans. Pattern Anal. Mach. Intell.*, vol. 22, no. 8, pp. 888–905, Aug. 2000.
- [38] D. Smith, G. Neumann, R. Arvidson, E. Guinness, and S. Slavney, "Mars global surveyor laser altimeter mission experiment gridded data record," *NASA Planetary Data System*, 2003. (MGS-M-MOLA-MEGDR-L3-V1.0).
- [39] T. Stepinski and R. Vilalta, "Digital topography models for Martian surfaces," *IEEE Geosci. Remote Sens. Lett.*, vol. 2, no. 3, pp. 260–264, Jul. 2005.
- [40] T. F. Stepinski, S. Ghosh, and R. Vilalta, "Automatic recognition of landforms on Mars using terrain segmentation and classification," in *Proc. Discov. Sci.*, 2006, pp. 255–266.
- [41] T. F. Stepinski, S. Ghosh, and R. Vilalta, "Machine learning for automatic mapping of planetary surfaces," in *Proc. 19th Innovative Appl. Artif. Intell. Conf.*, 2007, pp. 7–18.
- [42] K. L. Tanaka, "The Venus Geographic Mappers' Handbook," U.S. Geol. Surv., Flagstaff, AZ, Open File Rep. 99-438, 1994.
- [43] J. Theiler, "A contiguity-enhanced k-means clustering algorithm for unsupervised multispectral image segmentation," *Proc. SPIE*, vol. 3159, pp. 108–118, 1997.
- [44] R. Vilalta and T. F. Stepinski, "Thematic maps of Martian topography generated by a clustering algorithm," in *Proc. Lunar Planet. Inst. Conf. Abstr.*, S. Mackwell and E. Stansbery, Eds., 2004, pp. 1169–1170.
- [45] V. Walter, "Object-based classification of remote sensing data for change detection," *ISPRS J. Photogramm. Remote Sens.*, vol. 58, no. 3/4, pp. 225–238, Jan. 2004.
- [46] J.-P. Wang, "Stochastic relaxation on partitions with connected components and its application to image segmentation," *IEEE Trans. Pattern Anal. Mach. Intell.*, vol. 20, no. 6, pp. 619–636, Jun. 1998.
- [47] P. G. Wetzler, R. Honda, B. Enke, W. J. Merline, C. R. Chapman, and M. C. Burl, "Learning to detect small impact craters," in *Proc. 7th IEEE WACV/MOTION*. Washington, DC: IEEE Comput. Soc., 2005, vol. 1, pp. 178–184.
- [48] D. E. Wilhelms, "Geologic mapping," in *Planetary Mapping*. New York: Cambridge Univ. Press, 1990, pp. 208–260.
- [49] I. H. Witten and E. Frank, *Data Mining: Practical Machine Learning Tools and Techniques*, 2nd ed. ser. Morgan Kaufmann Series in Data Management Systems. San Francisco, CA: Morgan Kaufmann, 2005.



**Soumya Ghosh** is currently working toward the Ph.D. degree in the Department of Computer Science, University of Colorado at Boulder.

His research interests include exploring the intersection of machine learning and computer vision. He is interested in identification, recognition, and characterization of objects in cluttered natural scenes and in combining these algorithms to achieve higher level artificial-intelligence tasks such as image understanding. His current work focuses on developing machine-learning solutions to problems in mobile robotics.



**Tomasz F. Stepinski** received the Ph.D. degree in applied mathematics from the University of Arizona, Tucson.

He is a Planetary Scientist and is currently a Research Staff Member with the Lunar and Planetary Institute, Houston, TX. His main area of research is in automated identification, characterization, and classification of landforms, particularly on the planet Mars. He leads the planetary science community in developing methods for automatic cataloging of impact craters and valley networks—which are prominent landforms on Mars.



**Ricardo Vilalta** received the M.S. and Ph.D. degrees in computer science from the University of Illinois at Urbana–Champaign, Urbana.

He is currently an Associate Professor with the Department of Computer Science, University of Houston. His research interests include machine learning, statistical-learning theory, data mining, and artificial intelligence.

Dr. Vilalta was the recipient of the Best Paper Award at the European Conference on Machine Learning in 2003 and the NSF Career Award in 2005.